

Lateral tunable liquid microlenses for enhanced fluorescence emission in microfluidic channels

This article has been downloaded from IOPscience. Please scroll down to see the full text article.

2012 J. Micromech. Microeng. 22 105010

(<http://iopscience.iop.org/0960-1317/22/10/105010>)

View [the table of contents for this issue](#), or go to the [journal homepage](#) for more

Download details:

IP Address: 128.104.180.55

The article was downloaded on 27/08/2012 at 17:38

Please note that [terms and conditions apply](#).

Lateral tunable liquid microlenses for enhanced fluorescence emission in microfluidic channels

Ye Liu¹, Bader Aldalali¹ and Hongrui Jiang^{1,2,3,4}

¹ Electrical and Computer Engineering, University of Wisconsin—Madison, Madison, WI 53706, USA

² Biomedical Engineering, University of Wisconsin—Madison, Madison, WI 53706, USA

³ Materials Science Program, University of Wisconsin—Madison, Madison, WI 53706, USA

⁴ Eye Research Institute, University of Wisconsin—Madison, Madison, WI 53706, USA

E-mail: hongrui@engr.wisc.edu

Received 13 July 2012

Published 23 August 2012

Online at stacks.iop.org/JMM/22/105010

Abstract

Microlenses are important components of optofluidics systems and their lab-on-a-chip applications. We report on liquid microlenses that can be *in situ* formed in microchannels in a single batch via pneumatic control. These microlenses have optical axes that are parallel to the substrate, and their focal length can be pneumatically tuned separately and independently. In addition, the microlenses can also be pneumatically removed individually and reformed on demand. The parameters affecting the profiles and optical properties of the microlenses, such as the pressure difference and gravity, were investigated by simulation. We then demonstrated the enhancement of fluorescence emission in a microfluidic channel using our microlenses to focus attenuated excitation laser beams into regions of interest in the channel. With the microlenses, the region with visible fluorescence response was enlarged by up to 13 times and the intensity of fluorescence emission was enhanced by up to 38 times, compared to the cases without the lenses.

(Some figures may appear in colour only in the online journal)

1. Introduction

Optofluidics is a rapidly developing area that combines the advantages of microfluidics and optics [1]. Important applications of optofluidics include optofluidic dye lasers [2], liquid-core/liquid-cladding waveguides [3], and especially, lab-on-a-chip (LoC) systems [4–6]. Optofluidic LoC systems not only have many advantages inherited from their microfluidic attributes, such as portability, low-cost and low consumption of analytes and reagents, but also have advantages such as accuracy and remote controllability, inherited from their optic system aspects.

Microlenses, as one of the important components of optofluidic LoC systems, have been intensively investigated recently and utilized in many applications [7–10]. Solid-interface microlenses have been integrated into microfluidic chips through photoresist reflow [11], isotropic etching [12], chemical synthesis [13] and self-assembly processes [14].

However, these solid-interface microlenses are generally fixed in their shapes and thus not tunable in their focal lengths. For LoC applications, due to the requirements of compactness and versatility, tunable focal length of microlenses is not only an advantage, but also sometimes a necessity [15]. Tunable microlenses can be realized through various approaches, including reorientation of liquid crystals [16], electrowetting [17], mechanical actuation of polymeric materials [18], hydraulic pressure [19] or mechanical pressure [20], flow-rate-introduced shape change of the interface between two immiscible fluids [21–23] and self-adaptation to environmental parameters using responsive polymers [24–27]. These liquid-based lenses also have additional advantages such as smoother lens surfaces. However, many of these tunable microlenses rely on costly/complicated fabrication processes, various functional materials and complicated external hydrodynamic control systems. Most of them are also difficult to be removed and reformed on

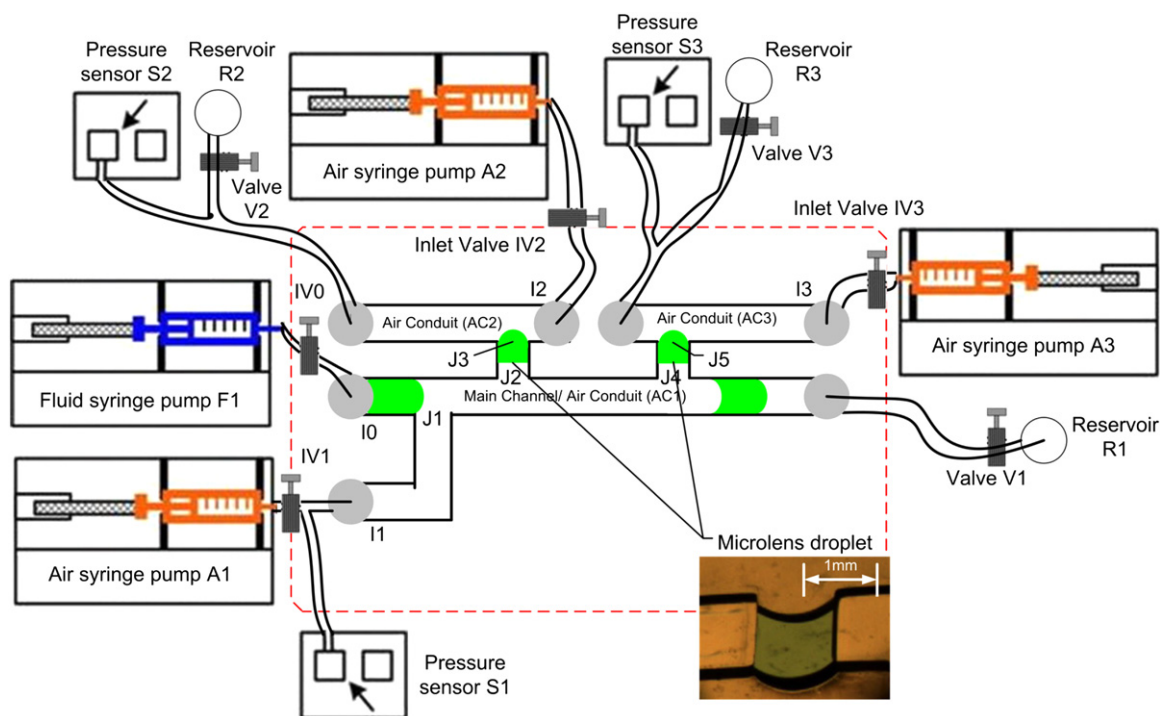


Figure 1. Schematic of the microfluidic setup for *in situ* formation of two microlenses. The widths of all microchannels were 1 mm except for the channel segments between junctions J2 and J3, and between J4 and J5, which were 0.75 mm. The depths of the channels were kept uniform at 250 μm .

demand. Moreover, most of these lenses have their optical axes perpendicular to the substrates (i.e. vertical lenses) so that other optical components involved (e.g., light sources and photodetectors) have to be laid out in different layers, which increases the difficulty in the integration and alignment of the components. Novel mechanical-wetting-based lenses have also been demonstrated [28, 29] with a relative low-cost and simple approach; however, the sizes of the lenses are relatively large (~ 7 mm).

We previously reported cylindrical liquid microlenses that are *in situ* formed and integrated within microfluidics through the pneumatic manipulation of fluids inside microchannels. Such microlenses are formed via liquid–air interfaces of liquid droplets, which are pinned at T-shaped junctions of channels. Via pneumatic control, these microlenses can uniquely be repositioned, removed, and reformed at predetermined locations within microchannels on demand. Moreover, their focal lengths can be tuned in a large range, from several micrometers to infinity, along the microchannels parallel to the substrate [30, 31].

To further extend our investigation on such pneumatically-controlled microlenses, we hereby report on *in situ* formed microlenses realized through an extended and improved fabrication and pneumatic control process. Compared to previously-reported single microlenses [30], multiple lateral microlenses with different optical axes were formed in one batch. The focal length of each microlens can be pneumatically tuned separately and independently, thus being more flexible in applications. The microlenses also inherit the advantages such as large range of tuning, ability to be removed and reformed, smooth surface, simple fabrication process,

and minimal requirement of external control systems once formed and sealed. More characterizations of the microlenses were performed, such as simulations of the focal length of the lenses as a result of the pneumatic tuning process, examination of the effect of gravity on the shape of the lenses and the optical properties of the microlenses. To further demonstrate their potential applications in LoC, we also demonstrated the enhancement of fluorescence excitation in microfluidic channels with the microlenses.

2. Formation, tuning, removal and reformation of the tunable liquid microlenses

2.1. Principles and structures

In a microfluidic channel network, the inner surfaces of the channels can be properly treated to form a hydrophobic monolayer, which is essential for the liquid–air interface to be perpendicular to both the top and bottom surfaces. Then, to form *in situ* tunable liquid microlenses, liquid droplets (here de-ionized, or DI, water) are pneumatically segmented from a static bulk fluid and then driven along the designated channels to desired T-shape junctions under controlled air pressure. Each of such droplets usually has two liquid–air interfaces, one of which would be pinned at the T-junction. This concept is depicted in figure 1.

When a difference in air-pressure is applied to the droplet and equals the internal capillary pressure caused by the difference in curvature between the liquid–air interfaces of the droplet, the liquid–air interface at the junction could protrude out of the junction, and be pinned at the edges—i.e. it tends to form a convex meniscus. The shape of the other

interface depends on the static contact angle of the liquid on the inner channel surface under homogeneous pneumatic pressure ([31], also see section 3.1). Thus, owing to the treated inner surfaces of the channels, it can be flat, forming a plano-convex cylindrical lens, or concave, forming a positive meniscus lens (with a larger radius of curvature than the convex surface). Such lenses have optical axes parallel to the substrate plane. Because of the ‘pinning’ effect at the junction, the curvature of the pinned liquid–air interface can be adjusted by varying the difference in the air pressure across the two liquid–air interfaces within a certain range.

2.2. Microfluidic system setup

As shown in figure 1, middle section, to form a multiple microlenses, a channel network was designed comprising of a main channel and multiple air conduits (for tuning), with lens channels between them, where the droplets of the liquid microlenses resided. The main channel was the place for forming the DI water droplets and driving them towards the junctions; it also served as an air conduit in the tuning process (AC1). Therefore, it had two inlets, one for the bulk fluid (I0) and one (I1) for the air plug to cut the droplets at J1. The air conduits provided the pneumatic control path for the lenses, thus each of them had an inlet for air (I2 and I3). The junctions (J2 and J3, J4 and J5) between the main channel, the air conduits, and the lens channels served as the designated pinning positions for the lens droplets.

The volumes and flow rates of air or DI water injected to the channel networks were controlled by syringe pumps (270810C, Cole-Parmer, Vernon Hills, IL, USA), and the pressure in each air conduit was monitored by pressure sensors (142PC30D, Honeywell, Morristown, NJ, USA). The inlets of the microfluidic channel network (I0, I1, I2 and I3) were connected to the syringe pumps via vinyl tubings (1/32 inch inner diameter, 3/32 inch outer diameter, Cole-Parmer Vernon Hills, IL, USA). For two lenses, four syringe pumps and three pressure sensors were used to allow for individual and independent tuning of each lens. As the formation and tuning process of each microlens is de-coupled, it is highly possible to integrate multiple microlenses into an array. Each lens in the array would require one syringe pump and one pressure sensor. Hence, for an n -lens array, $n+2$ syringe pumps and $n+1$ pressure sensors (including the main channel) would be needed.

The dimensions of the channel network for two microlenses, as shown in figure 1, are listed as follows. The width of all channels was 1 mm, except for that of the lens channels between J2 and J3, and between J4 and J5, which was 0.75 mm. The distances between J1 and J2, J2 and J3, J3 and J4 and J4 and J5 were 2.5, 1, 3 and 1 mm, respectively. The depths of the channels were kept uniform at 250 μm . DI water (dyed in green for easy observation) was prepared in a syringe and delivered through I0, while air was also kept in syringes and infused or withdrawn through I1, I2 and I3. The outlet of each air conduit was also connected to a waste reservoir through a controlling valve. Each inlet or outlet had a valve (inlet valves IV0, IV1, IV2, IV3 and valves V1, V2 and V3). The pressure

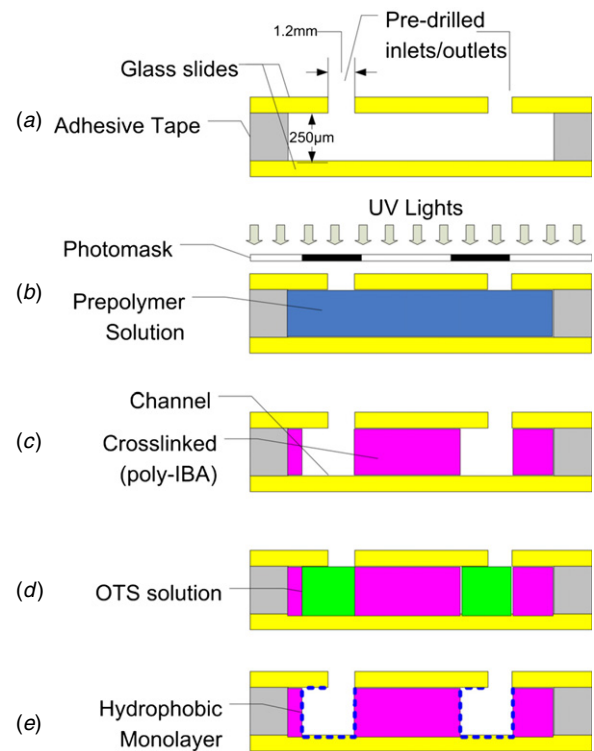


Figure 2. Fabrication process of microfluidic channels using LP³ based on UV photolithography with a single photo mask.

sensing range and the sensitivity of the pressure sensors were 0–30 lbf/in² and 166.7 mV/(lbf/in²), respectively.

2.3. Fabrication of microfluidic channels

The microchannel network was fabricated through a single-mask liquid-phase photopolymerization (LP³) process without the need for a clean room [32–34]. The photosensitive prepolymer solution used to form the channels was isobornyl acrylate (IBA). The solution consisted of three constituents in the following ratios: 31.66: 1.66: 1.0—monomer-IBA, crosslinker-tetraethylene glycol dimethacrylate (Sigma-Aldrich, Inc., St. Louis, MO) and photoinitiator-2,2-dimethoxy-2-phenylacetophenone (Sigma-Aldrich, Inc., St. Louis, MO).

As shown in figure 2(a), a chamber was created by attaching a polymer fluidic cartridge (Grace Bio-Labs, Bend, OR, USA) onto a pre-cleaned glass slide. The depth of the chamber was 250 μm . The inlets and outlets of the device (1.2 mm in diameter) were previously drilled on the cartridge with a mechanical driller. To improve the adhesion between the cartridge and the glass, the device was baked on a hot plate at 50 °C for 5 min. Then, the IBA-based prepolymer was flowed into the chamber and degassed for 10 min to remove bubbles. Afterwards, the microchannels were patterned inside the chamber by exposing it under an ultraviolet (UV) light (A4000, EXFO, Mississauga, Ontario, Canada) with an intensity of 7.8 mW cm⁻² for 24s, using a single photo mask film (Imagesetter Inc., Madison, WI, USA) (figure 2(b)). The device was then developed in a bath of ethanol for 100s,

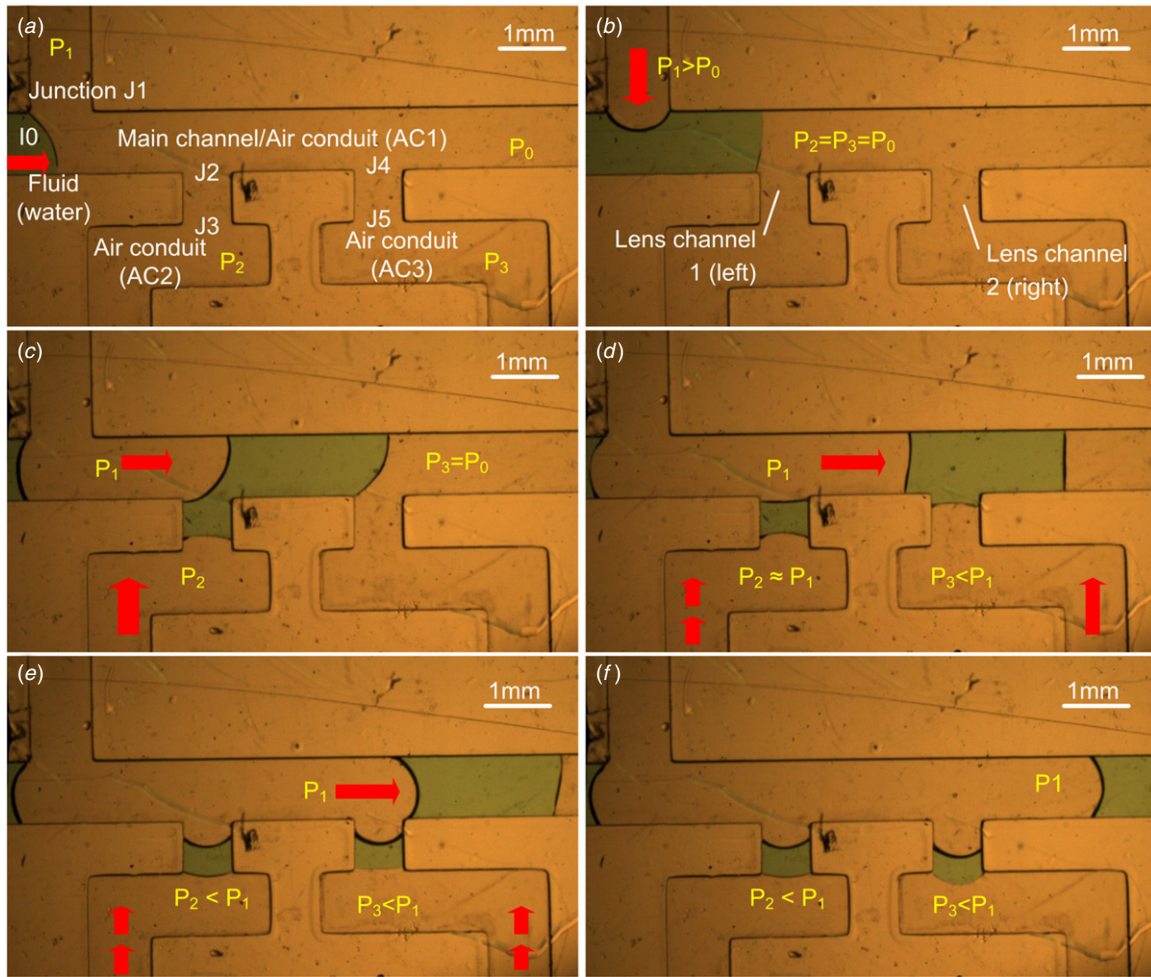


Figure 3. *In situ* formation process of two microlenses within the microchannel network. DI water was dyed green for easier observation.

then dried by nitrogen flow (figure 2(c)). For the purpose of surface chemical treatment, an octadecyltrichlorosilane (OTS) solution diluted by hexadecane [0.15% (v v⁻¹)] was flowed into the microchannels through an inlet and filled the whole channel for 3 min. After that, a peristaltic pump was used to flush away the solution, followed by flushing with a massive amount of isopropanol and drying. Thus, a self-assembled monomer hydrophobic layer was formed on the top surface, bottom surface and sidewalls of the channels, as shown in figure 2(e).

Compared to our previously reported fabrication approach, this modified process has several advantages. Instead of creating the chamber with two hard glass slides, the use of the flexible polymer cartridge greatly improved the adhesion between the cross-linked IBA and the inner top surface of the chamber, thus improving the air tightness of the fabricated device. Instead of using a massive amount of methanol to flush away the OTS/ hexadecane solution, we used a peristaltic pump to exhaust the solution first, thus preventing the contact of alcohol with hexadecane phase, which might cause the alcohol self-association phenomenon [35], forming aggregates that clog the microscale channels.

2.4. *In situ* formation of liquid microlenses

Figure 3 shows the formation process of two liquid microlenses. At the beginning, all inlet valves (IV0, IV1, IV2 and IV3) and V1 were open, while V2 and V3 were closed. As a result, the initial air pressure in the channels was set at $P_0 = 1$ atm. A bulk fluid (DI water, dyed green) was injected through I0 (figure 3(a)) with a flow rate of $5 \mu\text{L min}^{-1}$. After the fluid passed junction J1, the air pressure in air conduit AC1 was gradually increased in steps of 10 Pa, by periodically infusing air with a flow rate of $4.7 \mu\text{L min}^{-1}$ through I1 (figure 3(b)). The air infusion was paused for 10 s between each infusion step of 10 Pa to balance the pressure in the channel. As a result, a small droplet of the fluid was segmented from the bulk fluid. It was found that for this device, a minimal air pressure of $P_1 = P_0 + 390$ Pa was needed to completely cut and begin to drive a droplet of $\sim 0.88 \mu\text{L}$ in the main channel.

With the increase in P_1 , the droplet arrived at junction J2 and split at J2. A small portion of the droplet was left in the channel from J2 to J3, while a larger portion of the droplet was further driven towards J4 (figure 3(c)). As discussed in [30], the volume ratio of the smaller portion to the larger portion was proportional to the air pressure difference ratio $(P_1 - P_2)/(P_1 - P_0)$. Air infusion through AC1 was then paused

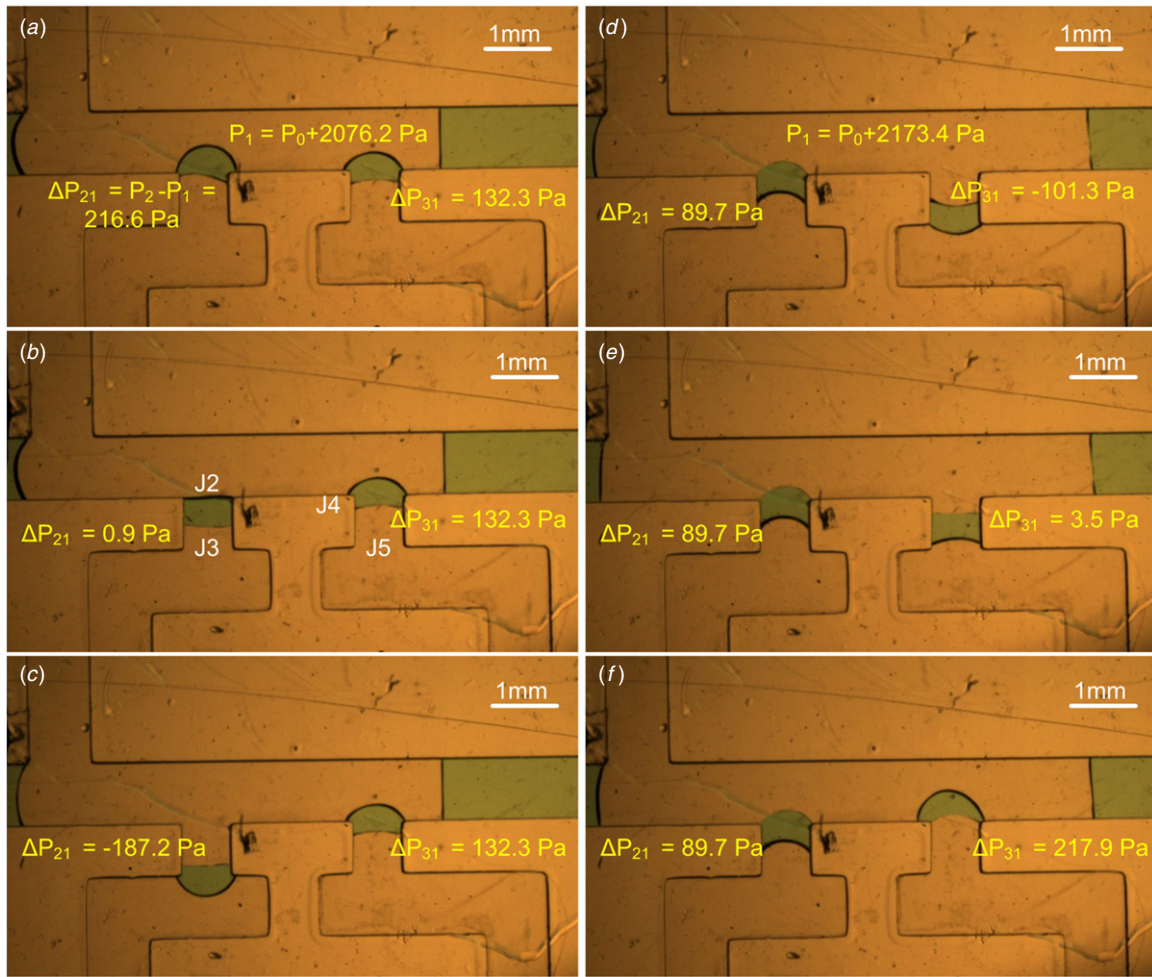


Figure 4. Individual tuning of each liquid microlens without affecting the other one.

and P_1 was maintained at $\sim P_0 + 900$ Pa, and an air plug was infused through AC2 to increase P_2 to $P_0 + 750$ Pa, leaving $0.15 \mu\text{L}$ of water between J2 and J3 and forming a lens droplet. Air infusion through AC1 was then restarted and the split was completed after P_1 was increased to $\sim P_0 + 930$ Pa.

The remaining droplet in the main channel was further driven by P_1 towards J4 (figure 3(d)). A similar splitting process occurred after P_1 was increased to $\sim P_0 + 2020$ Pa (figure 3(e)). P_3 was adjusted to $P_0 + 1660$ Pa so that $0.13 \mu\text{L}$ of water was left between J4 and J5, forming another lens droplet. To prevent the pressure differences between the two air-liquid interfaces of the droplet at J3 from exceeding the critical pressure difference (the pressure difference above which the droplet tends to be pushed to leave the junction; theoretical value: 219 Pa [31], experimental value: 217 ± 4 Pa), $\Delta P_{12} = P_1 - P_2$ was kept below 210 Pa, by air infusion through AC2 after each increasing step of P_1 . For the same reason, P_3 was increased immediately after splitting to $P_0 + 1830$ Pa and ΔP_{13} was kept below 210 Pa. Figure 3(f) depicts the final stage of the formation process of the lenses. P_1 was about $P_0 + 2180$ Pa. The profile of each lens can also be tuned pneumatically, which will be discussed in the next section.

After the formation of the lenses, all the valves at the inlets and outlets were closed and thus the channel network was sealed. The chip with the microlenses could then be detached

from the syringe pumps for storage or transfer. The shelf life of our microlenses device, using DI water as the lens liquid without refined air-tight package, is approximately one week before the volume of the lens droplets significantly decreases due to evaporation.

2.5. Individual tuning of the liquid microlenses

After the lens droplets were delivered to the lens channels (channels between J2 and J3, J4 and J5, etc), the shape of the microlenses can be tuned by adjusting the pressure difference across their air-liquid interfaces. As shown in figures 4(a), (b) and (c), one of the lens droplets was pinned at junction J4, forming a positive meniscus lens, since the pressure difference across its two surfaces remained at 132.3 Pa, and the curvature of the lens droplet was held still. Meanwhile, the air pressure difference across the two surfaces of the lens droplet in the left lens channel (between J2 and J3) was decreased from 216.6 (figure 4(a)) to 0.9 Pa (figure 4(b)) by decreasing P_2 ; thus, the interface pinned at J2 changed its shape from convex to almost planar. Consequently, the focal length of the microlens in the left channel increased from 0.972 mm (calculated; see discussion in section 3.3) to almost infinity. Further decrease in the pressure difference caused P_1 to be larger than P_2 , and the lens droplet was pushed away from J2 and instead pinned at

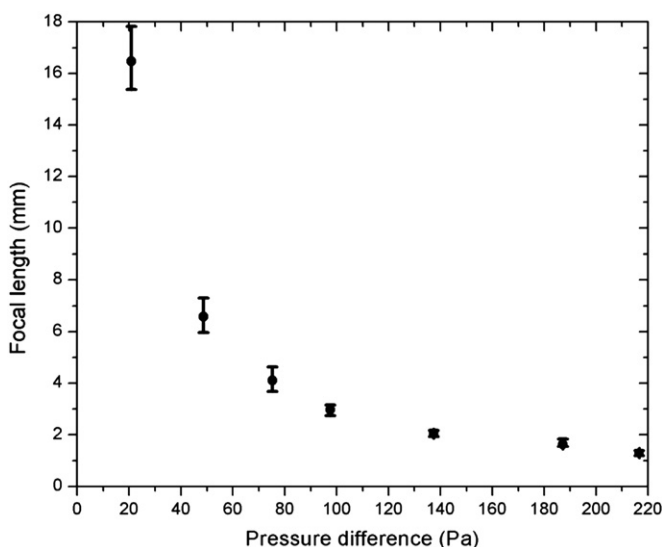


Figure 5. Relationship between the focal length of the microlenses and the pressure difference across the interfaces of the lens droplets. Pressure difference was recorded by monitoring the pressure sensors, while the profiles of the corresponding microlenses were recorded and parameters were fitted into a commercial simulation software to calculate the focal lengths (more details in section 3.3).

J3, forming another plano-convex lens (figure 4(c)). Similarly, figures 4(d)–(f) show the tuning process of the lens droplet in the right lens channel (between J4 and J5) by decreasing P_3 , while keeping the lens in the left lens channel unaffected.

The relationship between the focal length of the microlenses and the pressure difference across the lens droplet interfaces is plotted in figure 5. As expected, the focal length decreased rapidly with the increase in the pressure difference, as the increase in the pressure difference caused the decrease in the radius of curvature of a lens droplet. The focal length was approximately inversely proportional to the pressure difference, as indicated by the Young–Laplace equation (see section 3.2 for detail).

An important factor affecting the shape and the tuning of the microlenses is the contact angle of the droplet at different surfaces. The profiles of water droplets on glass, poly-IBA and cartridge treated by OTS as mentioned above were examined by a goniometer (OCA 5, Data Physics Instruments GmbH, Filderstadt, Germany) [30], and the contact angles were all estimated to be 90° . However, due to the hysteresis phenomenon of contact angles, this value was not absolute. There are also several non-ideal factors that affect the contact angle, such as the roughness of the channel surfaces and the quality/uniformity of the OTS monolayer on the surfaces. However, based on our observation and measurement by the goniometer, at the quasi-steady state, while only one interface was ‘pinned’ at a junction (such as the lenses in figures 4(b) and (c)), the contact angle of the droplet was within the range of 85° – 90° . Thus, for simplicity, we will assume the contact angle of the water droplets on the surfaces to be 90° in following experiments and simulations.

The shape of the liquid–air interface of a lens droplet, which is pinned at a junction of a lens channel, is determined by the Young–Laplace equation (see section 3.2). Meanwhile,

theoretically, the shape of the other ‘unpinned’ liquid–air interface depends on the static contact angle of the liquid on the channel material under homogeneous pneumatic pressure [30, 31]. This can be confirmed by a 2D computation fluidic dynamic simulation, discussed in section 3.1. However, situations were more complicated in the 3D experimental case. Since the tuning process was transient, the flow rate and the pneumatic pressure were not always homogeneous. The hydraulic pressure in the droplet was also largely uneven either. Thus, the shape of the other liquid–air interface, which was supposed to be flat, could be distorted during the pneumatic tuning process. As a result, instead of plano-convex microlenses, positive meniscus lenses were sometimes obtained. More analysis and experiments are needed to determine the condition needed to form plano-convex lenses and positive meniscus lenses.

2.6. Removal and reformation of the microlenses

One of the unique properties of the fabrication process and control scheme of our lenses was that the lenses can be removed individually and on demand. As shown in figures 6(a)–(c), keeping P_1 and P_3 unchanged while increasing P_2 , the lens pinned at J2 was gradually pushed out after the pressure difference ΔP_{21} exceeded the critical pressure (219 Pa), and was eventually removed from the junction. Meanwhile, the other lens at J4 was unaffected.

Another notable feature of our microlenses is that it provides a simple yet controllable way to remove all lenses in the microchannel network on demand. This was achieved by decreasing the pressure P_1 in AC1, while adjusting the pressure in other ACs. As shown in figures 6(d)–(f), P_1 was decreased from $\sim P_0 + 1950$ Pa to $\sim P_0 + 870$ Pa and then to $\sim P_0 + 20$ Pa in steps of ~ 10 Pa each, by withdrawing the air in AC1 at a rate of $4.7 \mu\text{L min}^{-1}$. The syringe pump was paused for 10 s between each step of withdrawal so as to keep the liquid quasi-stationary. When the droplet was moving along J4, P_3 was kept larger than P_1 to ensure that no liquid was left in the lens channels. Similarly, P_2 was kept larger than P_1 when the droplet was moving along J2. At the end of the withdrawal process, both microlens droplets were removed from the lens channels. This removal of the microlenses is complete as it would not leave any residual liquid except in the main channel, and thus did not require a subsequent cleaning process, which might introduce complexity to the air tightness of the system.

We then re-formed two lenses with a similar process as described in section 2.4. This time we adjusted P_2 and P_3 so that the liquid volume left in the lens channels was $\sim 0.16 \mu\text{L}$. The whole process was shown in figures 6(g)–(i).

3. Characterizations and simulations

3.1. Tuning of the microlens profiles

To investigate the relationship between the shape of the pinned microlens and the pressure difference across the interfaces of the lens droplet, a computation fluidic dynamic (CFD) simulation was performed with ANSYS Fluent[®] (version 12.0, ANSYS, Inc., Canonsburg, PA, USA). Instead of simply

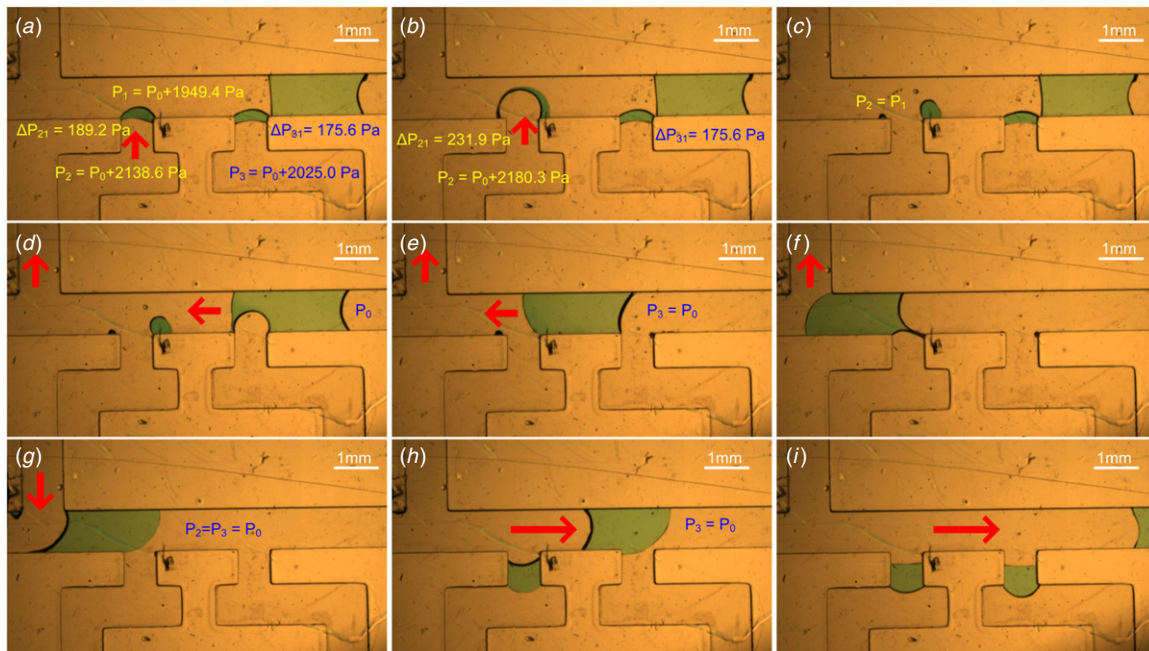


Figure 6. (a)–(c) Removal of a liquid microlens at J2 without affecting the other lens pinned at J3. (d)–(f) Removal of the microlenses. (g)–(i) Formation of new microlenses.

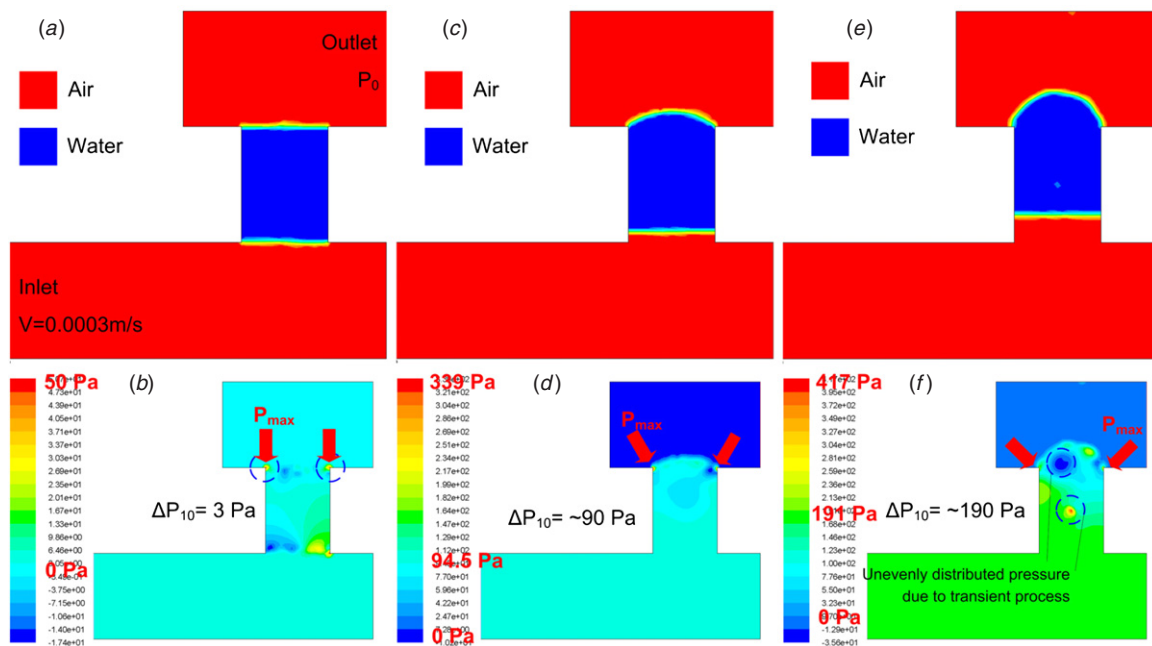


Figure 7. CFD simulation results of a microlens droplet in a channel network, pinned at a junction. (a), (c), (e) The shape change of the droplet with the increasing pressure. (b), (d), (f) The pressure distribution in the channel network.

evaluating the shape of one interface of the droplet using Young–Laplace equation, to accurately relate the pressure distribution inside the whole channel with the shape of the microlens from the top view, the simulation was performed as a transient analysis using a volume of fraction (VOF) model. To simplify the problem, the simulation was performed in 2D and the results are shown in figure 7. Consistent with the real case, a channel network with two air conduits (width: 1mm) and a lens channel (width: 0.75 mm) in between was defined, and one of the air conduits had an inlet while the other

had an outlet. The interacting liquid phases in this simulation were water and air, and the surface tension between them was set to be 75.64 dyn cm⁻¹. The contact angle between water and the channel walls was set to be 90°. At time instant 0, a droplet (0.1875 μL) was set to reside in the lens channel, and an air flow with a velocity of 0.0003 m s⁻¹ (corresponding to a volume velocity of 4.7 μL min⁻¹) was injected into the network through the inlet, while the pressure at the outlet was kept at 1 atm during the whole simulation process. Figures 7(a) and (b) depict the lens shape and the pressure distribution in

the channel after 10 ms of injection, where the surfaces were yet to change owing to the small pressure difference (only around 3 Pa). However, with the accumulation of the air in the inlet, the pressure in the air conduit with the inlet increased, pushing the lens droplet out of the lens channel. Combined with the pinning effect at the junction, the droplet protruded out and presented a convex lens. Figures 7(c) and (d) demonstrated this phenomenon. When the pressure difference approached 90 Pa after 2.4s of injection, the radius of curvature of the lens was approaching 0.92 mm (calculated from the profile of the liquid interface). After 6 s of injection, the pressure difference reached 190 Pa and the radius of curvature of the lens further decreased. According to figures 7(b), (d) and (f), the inner pressure of the droplet was increasing with the accumulation of the air, and the pressure difference across the ‘unpinned’ liquid–air interface was very small. The inner pressure of the droplet experienced a slow decrease from the ‘unpinned’ interface to the ‘pinned’ interface, while the liquid–air pressure decreased abruptly across the ‘pinned’ interface, as expected. The region with the largest pressure (pointed by arrows) appeared at the pinned edge of the droplet. Then, the air injection was stopped (air flow rate was set to 0), and after 800 ms, the shape of the droplet stopped changing, and we can consider that the quasi-steady state of the droplet was achieved. However, in the experiment where it is 3D in nature, according to our observation, it took much longer (10 s or more) for the droplet to experience small shape transitions and reach its quasi-steady state. Note that since the simulation uses a VOF model, the colorful boundary between water and air indicates the rapid change in the volume fractions of the two phases at the interface. Also note that the simulation was transient. Hence, figures 7(b), (d) and (f) show a transient pressure distribution, which is not homogeneous, and, as a result, the surfaces of the water droplet do not appear as smooth as those in the static state.

3.2. Effect of gravity

At the micro scale, gravity is generally dominated by surface tension and thus the shape of an air–liquid interface of a microlens droplet is determined by Young–Laplace equation [36]:

$$\Delta P = \gamma \left(\frac{1}{R_1} + \frac{1}{R_2} \right), \quad (1)$$

where ΔP is the pressure drop across the interface, γ is the liquid–surface free energy, and R_1 and R_2 are the principal radii of curvature of the interface. R_1 corresponds to the ‘top view’ of the air–liquid interface of a lens droplet, while R_2 corresponds to the ‘cross-section view’ along the optical axis of the lens droplet. Ignoring the effect of gravity and assuming fixed height of the channel, R_2 is inversely proportional to the contact angle of the liquid on the substrate (in our case, 90°). Thus, $1/R_2$ equals to 0 and R_1 has a simple relationship with ΔP :

$$R_1 = \gamma / \Delta P. \quad (2)$$

Equation (2) is only valid if the effect of gravity can be ignored. If gravity effect is comparable to the surface tension and pressure difference, R_2 cannot be considered

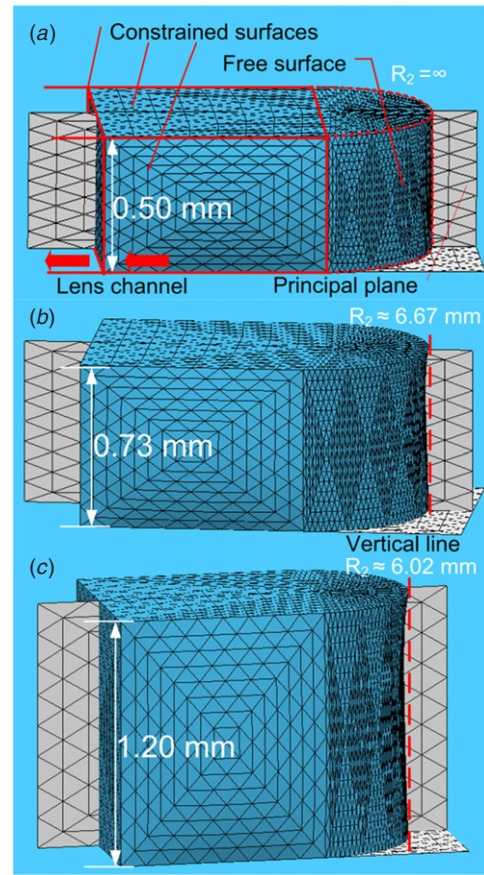


Figure 8. Simulation results of the steady state of cylindrical microlenses with different heights: (a) 0.50 mm, (b) 0.73 mm and (c) 1.20 mm. The distortion of the free surface was depicted by the principal plane intersecting the surface, and comparing the intersecting line with a line perpendicular to the substrate.

to be solely dependent on the contact angle at the liquid–substrate interface. A simulation using Surface Evolver (version 2.50, free software developed by Ken Brakke, Susquehanna University, Selinsgrove, PA, USA, available from <http://www.susqu.edu/brakke/evolverevolver.html>) is used to elucidate this effect and the results are shown in figure 8. We focused on examining the relationship between the heights of the droplets and the shapes of the free surfaces of the lens, when gravity is taken into account.

To adapt to the algorithm used by Surface Evolver, the problem was simplified to determine the shape of a free surface by the principle of minimum energy, considering the effect of gravity and other boundary conditions and constraints. To this end, a lens droplet in a lens channel with 1/3 of its volume protruding out of the channel and pinned at the junction was considered. The surfaces of the droplet inside the channel (confined in the framework of the solid red lines in figure 8(a)) were set to be stationary in all three dimensions, while the displacement degrees of freedom of the surface of the lens protruding out of the junction (depicted by the framework of the spotted red lines) were not confined. The contact angle between the liquid and the inner channel surface was set to be 90° , the density of the liquid was set to be 1 kg m^{-3} , and the gravity was set to be 9.81 m s^{-2} . Here, gravity was the

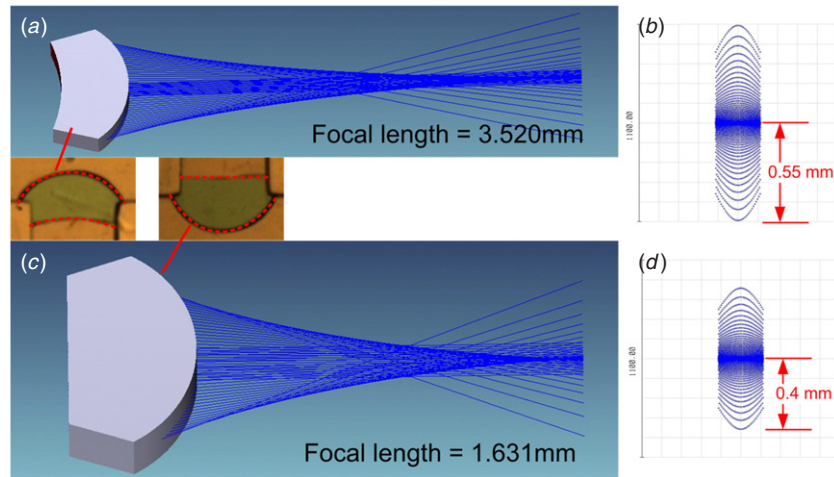


Figure 9. Ray-tracing simulation results of two cylindrical liquid microlenses. (a) Ray diagram of a positive meniscus lens whose profile matches the lens pinned at J4 in figure 4(c). (b) Spot diagram of the lens in (a) at its focus. (c) Ray diagram of a plano-convex lens matching the profile of the lens pinned at J3 in figure 4(c). (d) Spot diagram of the lens in (c) at its focus.

only parameter of interest; thus, the pressure within the liquid lens body and the pressure difference across the surfaces were not considered as constraints. The free surface evolved from a cuboid to the ultimate surface with the minimal free energy, as shown in figure 8. Comparing figures 8(a) and (c), gravity effect can be neglected when the height of the lens droplet is low (0.5 mm in figure 8(a)), and $1/R_2$ can be considered as 0. When the droplet height increases (figures 8(b) and (c)), under the gravity effect, the shape of the free surface is distorted and cannot be considered as perpendicular to the substrate, which affects the optical property of the liquid lens. Observing the shapes of the free surfaces of lenses with different heights, an empirical threshold of the height of the microlens was determined to be 0.73 mm to avoid distortion. At this height, the maximum deviation from the vertical line on the principal plane was estimated to be 0.01 mm; thus, R_2 can be estimated to be 6.67 mm. Similarly, R_2 approached 6.02 mm when the height of the droplet approached 1.20 mm.

3.3. Optical characterization

To investigate the optical properties of our lenses, a ray-tracing simulation was carried out using Zemax[®] (Radiat Zemax, Redmond, WA, USA). The results for two lenses are shown in figure 9 as examples. The profiles and dimensions of the lenses were measured from the fabricated lenses, and parameters such as radii of curvature of the interfaces were fitted from the obtained profiles. Here we focused on convex lenses. Two types of convex lenses were found in our microlenses assemblies: (1) positive meniscus lenses with one convex and one concave surfaces, with the radius of curvature of the convex surface being smaller than that of the concave surface; (2) plano-convex lenses with one convex surface and one planar surface. Figures 9(a) and (b) show the ray-tracing diagram and spot diagram of one positive meniscus lens, whose profile matches the lens at J4 in figure 4(c). The lens had a radius of curvature of 0.569 mm for the convex surface, a radius of curvature of -0.975 mm for the concave surface, and a thickness of 0.524 mm. Therefore, it had a focal length

of 3.52 mm and a lateral aberration of 0.55 mm. For the plano-convex lens at J3 in figure 4(c), its focal length was simulated to be 1.631 mm and the lateral aberration to be 0.4 mm.

4. Enhancing fluorescence emission in a microfluidic channel using lateral tunable liquid microlenses

It is a prevailing method to utilize fluorescence signals in LoC applications [8, 37, 38]. Conventionally, LoC chips containing the fluorescent materials, the stimulating light source and the fluorescence detection equipments are arranged in different vertical physical layers. However, this layout, as discussed before, may consume large spaces and introduce complexities in the miniaturization and integration. This problem can be alleviated if the stimulating light can be introduced from the lateral direction. However, the loss due to the sidewalls of the microfluidic channels or the mismatch in the coupling of optical fibers might greatly attenuate the stimulation light, thus affecting the feasibility of this design. By re-focusing the diffused/scattered light beam, our microlenses, however, provide an effective and controllable way to compensate for the attenuated stimulating light and to enhance the fluorescence emission.

To demonstrate this, an experiment of enhancing the fluorescence signal using our microlenses was performed (figure 10). The channel network to form the microlenses and a detection channel filled with fluorescein sodium salt solution ($10 \mu\text{M}$ in DI water) were integrated on the same glass slide. Two microlenses (figure 10, left corner) were formed through the process described in section 2.3. A blue laser (Laserglow Inc., Toronto, Canada, tunable intensity from 0~30 mW, spot size: ~ 1 mm) was used as the stimulating light source. The light beam was introduced into the microfluidic chip from a lateral direction. The laser beam was expanded with a $4\times$ beam expander (Newport, Irvine, CA, USA), and partially blocked by a shutter in the middle, in order to produce two laser beams with a width of ~ 1 mm to provide the light simultaneously to both microlenses. The

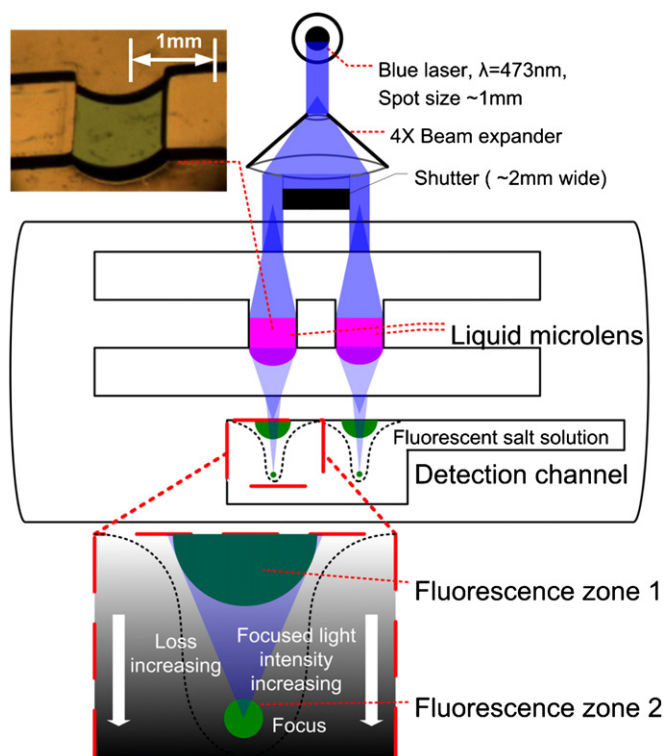


Figure 10. Setup for the experiment of using tunable lateral microlenses to enhance fluorescence emission in a microchannel.

beams (intensity before entering the chip: ~ 1.2 mW) passed through a layer of poly(IBA) sidewall and were focused into the detection channel by the microlenses. The fluorescent image was taken by a fluorescence microscopy camera (SMZ1500 with fluorescence module, Nikon, Melville, NY, USA). Due to the loss along the optical path in the detection channel, strength of the fluorescence signal would decrease rapidly. As a result, only a small zone close to the incoming light (labeled as ‘fluorescence zone 1’ in figure 10) exhibited visible fluorescence response without a lens or with a lens with a focal length of infinity (figure 11(a)). However, with the focusing power of the microlenses, the area of the zone

with visible fluorescence responses was enlarged and showed a stronger fluorescence emission, and the regions near the focused points of the microlenses (labeled as ‘fluorescence zone 2’ in figure 10, whose positions were adjustable) also showed visible fluorescence responses. By pneumatically adjusting the pressure difference across the interfaces of the lens droplets, thus changing the focal length of the microlenses, the area and intensity of the fluorescence zones could be controlled, as shown in figures 11(b) and (c). The focal length of the two lenses were tuned to approach infinity at first (figure 11(a)), then to 16.7 mm (figure 11(b)), and then to 6.9 mm and 8.1 mm, respectively (figure 11(c)). The corresponding maximum fluorescence emission (described by the local luminance in the image) in fluorescence zone 1s was increased from 68 (figure 11(d)) to 121 (figure 11(e)), then to 161 (figure 11(c)), indicating the enhancement of fluorescence signal. The fluorescence zone 2 of each microlenses could be moved separately (comparing figures 11(b) and (c)) by individually tuning the focal length of the microlenses. In doing so, the detection channel can be scanned along the optical axes of the microlenses, which could give a more detailed information about the distribution of the fluorescence-labeled analytes in the channel.

Fluorescence zone 1 of one microlens was observed under a high magnification to study the relationship between the focal length of the microlenses and the properties of fluorescence zone 1 (figure 12). To provide a more comprehensive view, parts of the lens channel and the lens droplet were also included in the images (the lens facet was depicted by the blue stimulating light scattered at the air–liquid interface). When there was no lens, or when the liquid lens had a focal length approaching infinity, only a small region (0.014 mm² in area, calculated from the fluorescence image, through the measurement module of ImageJ (open source software developed at National Institutes of Health, available at <http://rsbweb.nih.gov/ij/>), by estimating the ratio between a pixel and the area of real space, and then counting the pixels with an image luminance larger than 10) near the detection channel sidewall showed visible fluorescence response (figure 12(a)). Figure 12(b) shows the situation when the focal

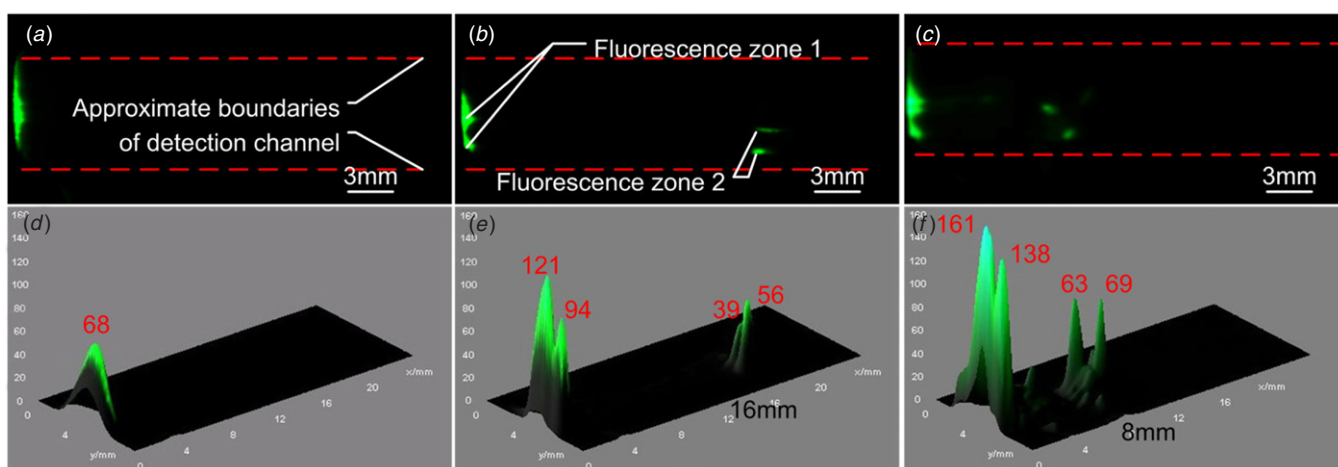


Figure 11. (a)–(c) Fluorescence response of a fluorescein sodium salt solution in the detection channel, corresponding to different focal lengths of the two microlenses, and (d)–(f) intensity of the fluorescence signal, represented by the local luminances of the image.

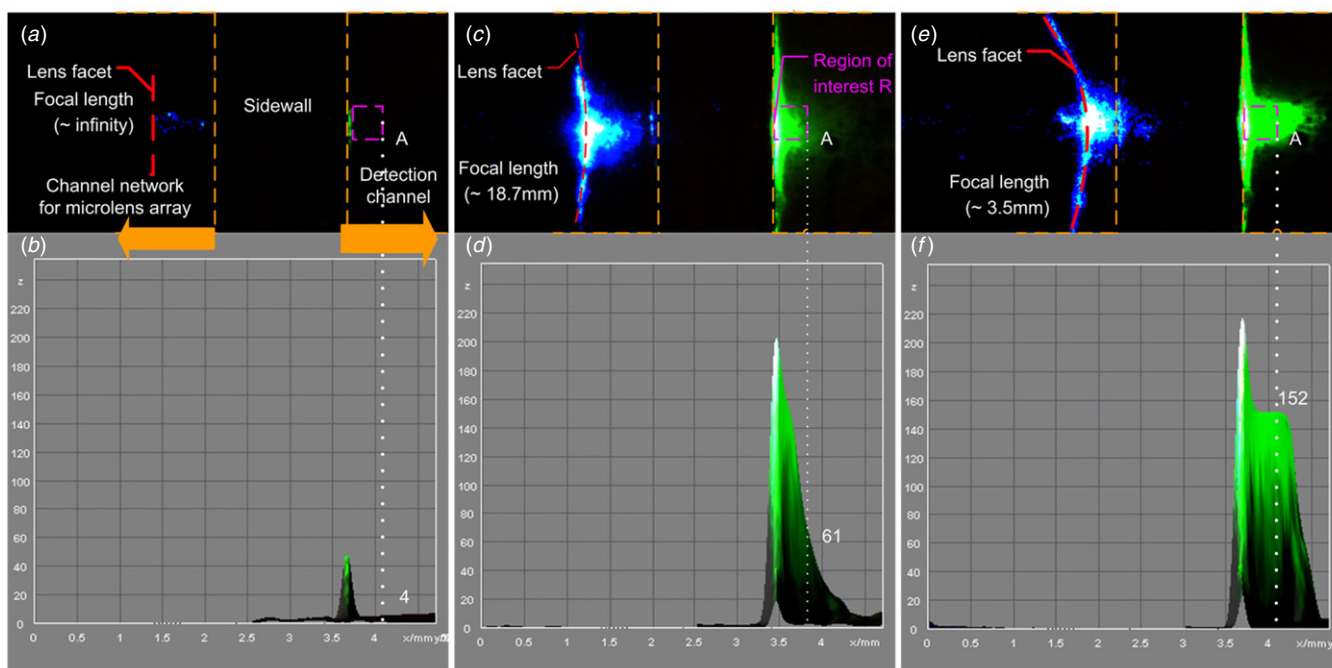


Figure 12. (a), (c), (e) Images of the microlens in its channel (left part) combined with the fluorescence image in the detection channel (right part). The sidewall between the two channels was marked by golden dashed lines. The lens facet (fitted by red dashed lines) can be observed from the scattered blue stimulating light. A region of interest 'R' near the detection channel sidewall (in fluorescence zone 1) was marked by pink dashed line, with its right corner annotated as 'A'. (b), (d), (f) The intensity of the fluorescence signal, represented by the local luminances of the image, corresponding to (a), (c), (e), respectively.

length was decreased to 18.7 mm, and the resultant area of the fluorescence zone 1 was increased to 0.097 mm^2 . When the focal length was further decreased to 3.5 mm (figure 12(c)), the area of fluorescence zone 1 was increased to 0.181 mm^2 , which was 13 times larger than that without a convex microlens. Considering a $0.3 \text{ mm} \times 0.3 \text{ mm}$ region near the sidewall of the detection channel (pink square 'R' in figure 12), without microlenses, fluorescence-labeled analytes inside this region could not be examined due to insufficient stimulating light. However, with the focusing of a tunable liquid microlens with a focal length of 3.5 mm, most of the analytes inside R can be stimulated by the blue light. Taking a point 'A' at the right corner of 'R' as an example, fluorescence signal strength at A was increased from 4 to 61 then to 152, increased by 38 times, with the decrease in the microlens focal length.

5. Conclusion

We have demonstrated lateral tunable liquid microlenses *in situ* formed in microchannel networks through pneumatic control. An optimized fabrication process was developed, and two microlenses were formed through pneumatic control. By adjusting the pressure differences across the interfaces of the microlens droplets, the lenses in the assembly can be individually tuned in focal length, removed, and re-formed on demand. Through simulation, the relationships between the profile/shape of the fabricated microlenses and factors such as pressure and gravity were examined. The optical properties of the lenses were also examined through a ray-tracing simulation. The potential applications of our microlenses in

lab-on-a-chip applications were also demonstrated by using it to enhance the fluorescence emission in an integrated detection channel. By tuning the focal length of our microlenses, the area of the fluorescence zones can be greatly enlarged (by 13 times), and the fluorescence signal can be effectively enhanced (by up to 38 times).

Future works include the optimization of the microlenses design and extending its applications. We will first integrate more microlenses into a single array and evaluate the limit in the number of microlenses in such an array. Secondly, we will integrate multiple liquid microlenses in one lens channel, which aligns the microlenses into a 2D array for more flexibility. Thirdly, more investigation will be carried out to determine when a pinned droplet will form a positive meniscus lens and when it will form a plano-convex lens. Then, we will also design and conduct more experiments to experimentally characterize the optical properties, such as the spherical aberration and coma of the microlenses, analyze the results, and compare them to the simulation results. Further, we will realize tracking of fluorescent particles in a microfluidic channel with the 2D-scanning capability of our microlenses.

Acknowledgments

This work is supported by the US Department of Homeland Security, through a grant awarded to the National Center for Food Protection and Defense at the University of Minnesota (grant number DHS-2007-ST-061-000003), the US National Science Foundation (grant ECCS 0622202) and the Wisconsin

Alumni Research Foundation. The authors thank Drs Liang Dong, Xuefeng Zeng and Daming Cheng for technical discussion.

References

- [1] Fainman Y, Lee L P, Psaltis D and Yang C 2009 *Optofluidics: Fundamentals, Devices, and Applications* (New York: McGraw-Hill)
- [2] Li Z Y, Zhang Z Y, Emery T, Scherer A and Psaltis D 2006 *Opt. Express* **14** 696–701
- [3] Wolfe D B, Conroy R S, Garstecki P, Mayers B T, Fischbach M A, Paul K E, Prentiss M and Whitesides G M 2004 *Proc. Natl Acad. Sci. USA* **101** 12434–8
- [4] Roulet J C, Volkel R, Herzig H P, Verpoorte E, de Rooij N F and Dandliker R 2001 *Opt. Eng.* **40** 814–21
- [5] Hubner J, Mogensen K B, Jorgensen A M, Friis P, Telleman P and Kutter J P 2001 *Rev. Sci. Instrum.* **72** 229–33
- [6] Jang J M, Shin H J, Hwang S W and Yang E G 2005 *Sensors Actuators B* **108** 993–1000
- [7] Carlson K, Chidley M, Sung K B, Descour M I, Gillenwater A, Follen M and Richards-Kortum R 2005 *Appl. Opt.* **44** 1792–7
- [8] Camou S, Fujita H and Fujii T 2003 *Lab Chip* **3** 40–5
- [9] Wendt J R et al 1999 *J. Vac. Sci. Technol. B* **17** 3252–5
- [10] Seo J and Lee L P 2004 *Sensors Actuators B* **99** 615–22
- [11] Yang H H, Chao C K, Wei M K and Lin C P 2004 *J. Micromech. Microeng.* **14** 1197–204
- [12] Savander P 1994 *Opt. Lasers Eng.* **20** 97
- [13] Wenger J, Gérard D, Aouani H and Rigneault H 2008 *Anal. Chem.* **80** 6800–4
- [14] Cayre O J and Paunov V M 2004 *J. Mater. Chem.* **14** 3300–2
- [15] Jiang H and Dong L 2006 *Phys. World* **19** 29–31
- [16] Presnyakov V V, Asatryan K E, Galstian T V and Tork A 2002 *Opt. Express* **10** 865–70
- [17] Kuiper S and Hendriks B H W 2004 *Appl. Phys. Lett.* **85** 1128–30
- [18] Zhang D Y, Lien V, Berdichevsky Y, Choi J and Lo Y H 2003 *Appl. Phys. Lett.* **82** 3171–2
- [19] Lee S W and Lee S S 2007 *Appl. Phys. Lett.* **90** 121129
- [20] Ren H and Wu S T 2005 *Appl. Phys. Lett.* **86** 211107
- [21] Mao X, Waldeisen J R, Juluria B K and Huang T J 2007 *Lab Chip* **7** 1303–8
- [22] Mao X, Lin S S C, Lapsley M I, Shi J, Juluria B K and Huang T J 2009 *Lab Chip* **9** 2050–8
- [23] Seow Y C, Liu A Q, Chin L K, Li X C, Huang H J, Cheng T H and Zhou X Q 2008 *Appl. Phys. Lett.* **93** 084101
- [24] Dong L, Agarwal A K, Beebe D J and Jiang H 2006 *Nature* **442** 551–4
- [25] Dong L, Agarwal A K, Beebe D J and Jiang H 2007 *Adv. Mater.* **19** 401–5
- [26] Dong L and Jiang H 2006 *Appl. Phys. Lett.* **89** 211120
- [27] Kim J, Serpe M J and Lyon L A 2004 *J. Am. Chem. Soc.* **126** 9512–3
- [28] Xu S, Liu Y, Ren H and Wu S T 2010 *Opt. Express* **18** 12430–5
- [29] Li L, Wang Q-H and Jiang W 2011 *J. Opt.* **13** 115503
- [30] Dong L and Jiang H 2008 *J. Microelectromech. Syst.* **17** 381–92
- [31] Dong L and Jiang H 2007 *Appl. Phys. Lett.* **91** 041109
- [32] Agarwal A K, Sridharamurthy S S, Beebe D J and Jiang H 2005 *J. Microelectromech. Syst.* **14** 1409–21
- [33] Agarwal A K, Beebe D J and Jiang H 2006 *J. Micromech. Microeng.* **16** 332–40
- [34] Beebe D J, Moore J S, Yu Q, Liu R H, Kraft M L, Jo B H and Devadoss C 2000 *Proc. Natl Acad. Sci. USA* **97** 13488–93
- [35] Tucker E E, Farnham S B and Christian S D 1969 *J. Phys. Chem.* **73** 3820–9
- [36] Atencia J and Beebe D J 2005 *Nature* **437** 648–55
- [37] Ibarlucea B, Fernandez-Rosas E, Vila-Planas J, Demming S, Nogues C, Plaza J A, Büttgenbach S and Llobera A 2010 *Anal. Chem.* **82** 4246–51
- [38] Sedgwick H, Caron F, Monaghan P B, Kolch W and Cooper J M 2008 *J. R. Soc. Interface* **5** S123–30